Computer Methods in Applied Mechanics and Engineering 450 (2026) 118642

Contents lists available at ScienceDirect

Comput. Methods Appl. Mech. Engrg.

journal homepage: www.elsevier.com/locate/cma

Adaptive finite element phase-field simulation of dynamic brittle fracture

Hossein Saberi *, Alexander Düster

Hamburg University of Technology, TUHH, Numerical Structural Analysis with Application in Ship Technology (M-10), Am Schwarzenberg-Campus 4 (C), Hamburg, 21073, Germany

ARTICLE INFO

Keywords:
Adaptive mesh refinement
Finite element method
Phase-field method
Dynamic fracture
Damping effects

ABSTRACT

In finite element analysis, mesh refinement is typically employed to improve accuracy by increasing spatial resolution in regions with steep solution gradients. This study presents an adaptive mesh refinement technique for dynamic fracture simulation based on the phase-field method. A multi-level node distance function is introduced using the phase-field variable to control mesh density. As damage evolves, the nodal spacing is adaptively refined according to the prescribed maximum spacing; whenever the computed distance exceeds this threshold, a new field node is introduced at the element center, ensuring the mesh evolves consistently with crack propagation. In addition, material damping effects are incorporated into the phase-field formulation to capture realistic dynamic fracture responses. Time integration is investigated using the Newmark scheme, the generalized-α method, and the backward implicit approach. The results indicate that, while the first two schemes are commonly applied, the backward implicit method provides superior stability in dynamic simulations. Furthermore, a staggered solution strategy is proposed in which both displacement and phase-field variables are iteratively and consistently updated within each solution step. The effectiveness of the proposed methodology is demonstrated through three numerical examples. The responses of elastic energy, kinetic energy, and energy dissipated by crack propagation are evaluated, together with the effects of material damping. The results confirm that the presented approach significantly improves computational efficiency while preserving accuracy and exhibits robust convergence behavior in highly dynamic fracture simulations.

1. Introduction

Fracture is one of the most prevalent failure mechanisms in engineering materials and structures, making it a subject of extensive research since the foundational studies of [1]. As highlighted in [2], fracture inherently involves dynamic processes at some scale due to the nature of bond rupture, which is why dynamic fracture is a fundamental aspect of fracture mechanics. In practice, dynamic fracture plays a crucial role in various scenarios, such as impact damage in automobiles, aircraft windshields, etc. The analysis of dynamic fracture relies on the principles of fracture mechanics, where inertial effects become significant. These effects may result from either rapidly applied external loads or fast crack propagation, where the crack velocity approaches the material's Rayleigh wave speed and may reach several thousand meters per second, even under quasi-static loading conditions. Since analytical solutions are only available for a limited set of simplified cases, researchers frequently rely on experimental and computational approaches to gain deeper insight into dynamic fracture phenomena. While experiments provide valuable data, they are often expensive and

* Corresponding author.
E-mail addresses: hossein.saberi@tuhh.de (H. Saberi), alexander.duester@tuhh.de (A. Düster).

https://doi.org/10.1016/j.cma.2025.118642
Received 22 September 2025; Received in revised form 7 November 2025; Accepted 1 December 2025
Available online 16 December 2025

time-intensive [3]. Numerical simulations serve as a complementary tool, offering detailed insights into spatial and temporal scales that are otherwise challenging or impossible to observe experimentally. Despite significant progress, several challenges persist in this area: (i) establishing effective formulations and numerical strategies to accurately capture crack initiation, propagation, and interaction in porous materials; (ii) enhancing computational efficiency to facilitate large-scale engineering applications; and (iii) designing advanced numerical schemes capable of handling complex geometries, including structures with irregularly distributed pores [4]. In order to address these challenges, various numerical approaches have been developed over the past decades to simulate dynamic crack propagation. These approaches can be broadly divided into three main types: discrete, continuous, and hybrid methods. Several well-established theories have been developed for discrete approaches, including the discrete element method [5–7], cohesive zone models [8–10], peridynamics [11–14], and the extended finite element method (XFEM) [15,16], all of which allow displacement discontinuities along the fracture surface. In contrast, continuous approaches ensure displacement continuity throughout the domain while representing fracture through a gradual stress reduction, typically modeled using softening material laws. Among these, continuum damage mechanics is one of the most widely adopted frameworks for continuous fracture modeling [17]. To leverage the strengths of both discrete and continuous methods, various hybrid techniques have been introduced.

From a computational standpoint, many of the aforementioned approaches face challenges when handling complex crack patterns, such as branching, which complicates numerical implementation and often limits their applicability to simpler crack geometries. A promising alternative is the variational fracture approach [18,19], commonly referred to as the phase-field method. Variational phase-field fracture models (PFMs) extend Griffith's linear elastic fracture mechanics (LEFM) while sharing numerical similarities with continuum damage mechanics (CDM) [20,21]. These models offer several benefits associated with CDM, including the elimination of the need for explicit crack tracking, the absence of ad hoc dynamic branching criteria, and relatively straightforward implementation into standard C^0- continuous finite elements, specially when compared to discontinuous fracture models. The phase-field method is well-established and has been proven effective in modeling experimental data. Hug et al. [22] employed a modified phase-field method within the finite cell method (FCM) to simulate impacted fractures of the proximal humerus. The results demonstrated that PFM accurately predicts the force-strain response, failure loads, and fracture path, closely matching experimental observations, with a maximum relative error of only 3.8 % in failure loads. In another study, Hug et al. [23] employed distinct phase-field variables to model the combination of Mode I (tensile) and Mode II (shear) fractures in rocks. The model accurately simulates the crack patterns seen in double-edge notched Brazilian disk tests performed on Pfraundorfer Dolostone and Solnhofen Limestone.

Borden et al. [24] extended the quasi-static phase-field model of Miehe et al. [19] to dynamic fracture by formulating the Lagrangian in terms of displacements and the phase-field variable. Their analytical studies showed that the length-scale parameter governs the critical stress for crack nucleation. Using NURBS and T-spline basis functions, they compared monolithic and staggered schemes for flexible implicit or explicit time integration. Schlüter et al. [25] developed a dynamic phase-field model for brittle fracture based on Hamilton's principle, enabling simulation of crack initiation and branching due to stress waves. However, the method requires extremely fine meshes over the entire domain, making computations expensive. Nguyen and Wu [26] proposed a phase-field regularized cohesive zone model (PFCZM) for dynamic and quasi-brittle fracture. The model captures branching and fragmentation without crack tracking but remains computationally costly due to fine mesh requirements. Geelen et al. [27] extended a cohesive phase-field/gradient damage formulation to dynamic fracture using a regularized linear fracture energy and non-polynomial degradation functions. An augmented Lagrangian–based staggered scheme ensured efficiency, though convergence and parameter calibration remain open issues. Zhou et al. [28] introduced a phase-field model for fluid-driven dynamic fracture in poroelastic media, combining Biot's theory with phase-field regularization. While accurate and robust, it is computationally intensive and limited to homogeneous media. Ren et al. [29] developed an explicit dynamic phase-field model that alleviates convergence issues and simplifies stiffness computations compared to implicit schemes.

De Lorenzis and Gerasimov [30] reviewed the main computational challenges in phase-field modeling of brittle fracture, particularly the treatment of irreversibility and the iterative solution of non-convex minimization problems. They emphasized that adaptive mesh refinement (AMR) is a practical strategy for improving computational efficiency. While higher-order phase-field formulations can also reduce computation time [31], adaptivity remains the most widely used approach due to its simplicity and robustness for complex crack patterns. Patil et al. [32] developed the Adaptive Multiscale Phase-Field Method (AMPFM), which drastically reduces computational cost through a hierarchical coarse-to-fine mesh structure. However, its reliance on structured meshes limits its flexibility for complex geometries compared with general unstructured AMR schemes. Li et al. [33], and Si et al. [34] proposed adaptive isogeometric and hybrid FEM frameworks for dynamic brittle fracture, demonstrating the advantages of adaptivity in both quasi-static and dynamic regimes. Jin et al. [35] introduced a monolithic phase-field framework combining the limited-memory BFGS (L-BFGS) optimization method with AMR to overcome convergence issues of Newton-based solvers and enhance efficiency. Fine meshes are confined to crack regions, while hanging-node constraints are algebraically enforced to preserve conformity. Despite its accuracy, the approach remains computationally demanding due to constraint handling and multi-level refinement. Pandey [36] proposed an element-level hierarchical AMR strategy for the phase-field regularized cohesive zone model (PFCZM), refining the mesh adaptively near crack tips using multiple error indicators. The method eliminates hanging nodes and supports both structured and unstructured meshes, but still faces significant computational overhead from element-level refinement and indicator evaluation. Greco et al. [37] investigated low- and high-order phase-field models for dynamic brittle fracture, showing that fourth-order formulations enable coarser meshes and larger time steps without loss of accuracy. Building on this, Li et al. [4] proposed a fourth-order adaptive isogeometric phase-field model for dynamic fracture, which alleviates mesh-size constraints but exhibits oscillations likely due to convergence issues.

The main novelty of this study lies in extending our previously developed multi-level adaptive mesh strategy [38] to dynamic fracture problems for the first time. In this approach, FEM analysis is initially conducted on a coarse mesh. As the crack propagates,

new field nodes are progressively added to regions where finer meshes are required, reducing the node spacing accordingly. We also present a formulation incorporating damping effects in phase-field fracture problems and conduct a comprehensive analysis of the energy responses.

The paper is structured as follows: Section 2 presents the formulation of the phase-field method for dynamic crack propagation. Section 3 presents a detailed adaptive scheme and its numerical implementation. A comprehensive analysis of dynamic crack branching is given in Section 4. Finally, key findings are discussed in Section 5.

2. Phase-field model and its discretization

2.1. Governing equations

An initially fractured domain is subjected to body forces **b** and tractions **t** as shown in Fig. 1. The energy functional corresponding to a cracked domain assuming small deformations is expressed as:

$$L = \int_\Omega \psi^k(\boldsymbol{u})\, d\Omega + \int_\Omega \psi^e(\boldsymbol{\varepsilon}, d)\, d\Omega + \int_{\Gamma_c} G_c\, d\Gamma - \int_\Omega \boldsymbol{b}\cdot\boldsymbol{u}\, d\Omega - \int_{\Gamma_t} \boldsymbol{t}\cdot\boldsymbol{u}\, dS, \tag{1}$$

in which the linear strain tensor $\boldsymbol{\varepsilon}$ is defined as $\boldsymbol{\varepsilon} = \left(\nabla\boldsymbol{u} + \nabla\boldsymbol{u}^T\right)/2$, $\boldsymbol{u}$ represents the displacement field, and d denotes the phase-field variable. The kinetic energy density and the elastic strain energy density are denoted by $\psi^k(\boldsymbol{u})$ and $\psi^e(\boldsymbol{\varepsilon}, d)$, respectively.

The fracture energy can be approximated by a regularization [39] as:

$$\int_{\Gamma_c} G_c d\Gamma \approx \frac{G_c}{2\ell_0}\int_\Omega \left(d^2 + \ell_0^2 \nabla d\cdot\nabla d\right) d\Omega, \tag{2}$$

where $\nabla(\cdot)$ represents the gradient operator, G_c is the material fracture toughness, and ℓ_0 represents a length scale parameter that determines the crack width.

To ensure that stress degradation occurs solely under tensile conditions, the strain tensor is split into its tensile (positive) and compressive (negative) components. The elastic energy is derived from the positive (ψ_0^+) and negative (ψ_0^-) components of the strain tensor, which are defined via a spectral decomposition of the strain [19]:

$$\begin{aligned}
&\psi^e(\boldsymbol{\varepsilon}, d) = g(d)\,\psi_0^+(\boldsymbol{\varepsilon}) + \psi_0^-(\boldsymbol{\varepsilon}),\\
&\psi_0^+(\boldsymbol{\varepsilon}) = \frac{\lambda}{2}\langle \mathrm{Tr}(\boldsymbol{\varepsilon})\rangle_+^2 + \mu\,\mathrm{Tr}\left[(\boldsymbol{\varepsilon}^+)^2\right], \quad \psi_0^-(\boldsymbol{\varepsilon}) = \frac{\lambda}{2}\langle \mathrm{Tr}(\boldsymbol{\varepsilon})\rangle_-^2 + \mu\,\mathrm{Tr}\left[(\boldsymbol{\varepsilon}^-)^2\right],
\end{aligned} \tag{3}$$

$$\boldsymbol{\varepsilon} = \boldsymbol{\varepsilon}^+ + \boldsymbol{\varepsilon}^-, \quad \boldsymbol{\varepsilon}^+ = \sum_{i=1}^{3} \left\langle \varepsilon^i \right\rangle_+ \mathbf{n}^i \otimes \mathbf{n}^i, \quad \boldsymbol{\varepsilon}^- = \sum_{i=1}^{3} \left\langle \varepsilon^i \right\rangle_- \mathbf{n}^i \otimes \mathbf{n}^i, \tag{4}$$

where $\langle x\rangle_\pm = (x \pm |x|)/2$ and eigenvalues and eigenvectors of the strain tensor are denoted by ε^i and $\mathbf{n}^i$, respectively. $\mathrm{Tr}(\cdot)$ represents the trace operator, λ and μ are the Lamé constants. Additionally, $g(d) = (1-d)^2 + \kappa$ denotes the degradation function [40] in which κ is a small numerical parameter introduced to maintain the well-posedness of the stiffness matrix.

The kinetic energy reads:

$$\Psi^k(\dot{\boldsymbol{u}}) = \int_\Omega \psi^k(\dot{\boldsymbol{u}})\, d\Omega = \frac{1}{2}\int_\Omega \rho\, \dot{\boldsymbol{u}}\cdot\dot{\boldsymbol{u}}\, d\Omega, \tag{5}$$

in which the material density and velocity are denoted by ρ and $\dot{\boldsymbol{u}} = d\boldsymbol{u}/dt$, respectively.

The variation of Eq. (1) yields:

$$\delta L(\delta\boldsymbol{u}, d) = \int_\Omega \boldsymbol{\sigma} : \delta\boldsymbol{\varepsilon}\, d\Omega + \int_\Omega \rho\, \ddot{\boldsymbol{u}}\cdot\delta\boldsymbol{u}\, d\Omega - \int_\Omega \boldsymbol{b}\cdot\delta\boldsymbol{u}\, d\Omega - \int_{\Gamma_t} \boldsymbol{t}\cdot\delta\boldsymbol{u}\, dS = 0, \tag{6}$$

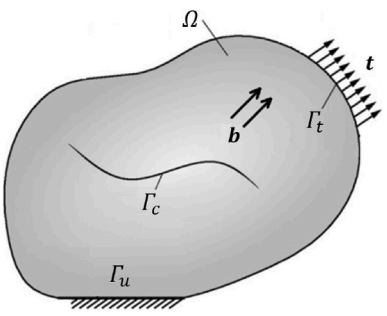

Fig. 1. Cracked body and boundary conditions.

$$\delta L(\boldsymbol{u},\delta d)=\frac{G_c}{\ell_0}\int_\Omega\left(d\cdot\delta d+\ell_0^2\nabla d\cdot\nabla\delta d\right)d\Omega-\int_\Omega 2(1-d)\delta d\,\psi_0^+\,d\Omega=0, \tag{7}$$

where the acceleration $\ddot{\boldsymbol{u}}$ and the stress tensor $\boldsymbol{\sigma}$ are defined as $\ddot{\boldsymbol{u}}=d^2\boldsymbol{u}/dt^2$ and $\boldsymbol{\sigma}=\frac{\partial\psi}{\partial\boldsymbol{\varepsilon}}=\frac{\partial}{\partial\boldsymbol{\varepsilon}}\left(g(d)\psi_0^+(\boldsymbol{\varepsilon})+\psi_0^-(\boldsymbol{\varepsilon})\right)=g(d)\frac{\partial\psi_0^+(\boldsymbol{\varepsilon})}{\partial\boldsymbol{\varepsilon}}+\frac{\partial\psi_0^-(\boldsymbol{\varepsilon})}{\partial\boldsymbol{\varepsilon}}$, respectively.

To impose the condition of damage irreversibility, the history function has been introduced as $\mathcal{H}_i(\mathbf{x})=\max_{i\geq1}\left\{\mathcal{H}_{i-1}(\mathbf{x}),\,\Psi_e^+(\boldsymbol{\varepsilon}(\boldsymbol{u}))\right\},\mathcal{H}_0=0$, as discussed in Ref [19].

2.2. Spatial discretization

In this section, the spatial discretization of the above equations in a two-dimensional setting is presented. The field displacement variable $\boldsymbol{u}$ and field damage variable d are approximated by

$$\boldsymbol{u}=\boldsymbol{N}_{\boldsymbol{u}}\boldsymbol{u}^e,\qquad d=\boldsymbol{N}_d\boldsymbol{d}^e, \tag{8}$$

$$\boldsymbol{N}_{\boldsymbol{u}}=[\boldsymbol{N}_{\boldsymbol{u}}^1\quad\boldsymbol{N}_{\boldsymbol{u}}^2\quad\dots\quad\boldsymbol{N}_{\boldsymbol{u}}^m],\qquad\boldsymbol{N}_{\boldsymbol{u}}^i=\begin{bmatrix}N^i&0\\0&N^i\end{bmatrix},$$

$$\boldsymbol{u}^e=[\boldsymbol{u}_1^{eT}\quad\boldsymbol{u}_2^{eT}\quad\dots\quad\boldsymbol{u}_m^{eT}]^T,\qquad\boldsymbol{u}_i^e=\begin{bmatrix}u_i^x\\u_i^y\end{bmatrix},$$

$$\boldsymbol{N}_d=[N^1\quad N^2\quad\dots\quad N^m],\qquad\boldsymbol{d}^e=[d_1^e\quad d_2^e\quad\dots\quad d_m^e]^T,$$

where N^i denotes the shape function associated with the i^{th} node and m denotes the number of field nodes. Moreover, the gradients are evaluated by the following expressions:

$$\boldsymbol{\varepsilon}=\boldsymbol{B}_{\boldsymbol{u}}\boldsymbol{u}^e,\qquad\boldsymbol{B}_{\boldsymbol{u}}=[\boldsymbol{B}_{\boldsymbol{u}}^1\quad\boldsymbol{B}_{\boldsymbol{u}}^2\quad\dots\quad\boldsymbol{B}_{\boldsymbol{u}}^m],\qquad\boldsymbol{B}_{\boldsymbol{u}}^i=\begin{bmatrix}N_{,x}^i&0\\0&N_{,y}^i\\N_{,y}^i&N_{,x}^i\end{bmatrix}, \tag{9}$$

$$\nabla d=\boldsymbol{B}_d\boldsymbol{d}^e,\quad\boldsymbol{B}_d=[\boldsymbol{B}_d^1\quad\boldsymbol{B}_d^2\quad\dots\quad\boldsymbol{B}_d^m],\quad\boldsymbol{B}_d^i=[N_{,x}^i\quad N_{,y}^i]^T, \tag{10}$$

where the terms $N_{,x}^i$ and $N_{,y}^i$ correspond to the partial derivatives in the directions of the global coordinates x and y, respectively. Inserting this ansatz into the variational formulation and considering the damping effects leads to the semi-discrete equation of motion:

$$\boldsymbol{M}\ddot{\boldsymbol{u}}+\boldsymbol{C}_d\,\dot{\boldsymbol{u}}+\boldsymbol{\Lambda}(\boldsymbol{u},d)=\boldsymbol{F}_{\boldsymbol{u}}, \tag{11}$$

$$\boldsymbol{M}=\mathcal{A}_{e=1}^{n_{\text{elem}}}\boldsymbol{M}^e,\quad\boldsymbol{M}^e=\int_{\Omega^e}\rho(\boldsymbol{N}_{\boldsymbol{u}})^T\boldsymbol{N}_{\boldsymbol{u}}\,dV,$$

$$\boldsymbol{C}_d=\mathcal{A}_{e=1}^{n_{\text{elem}}}\boldsymbol{C}_d^e,\quad\boldsymbol{C}_d^e=\alpha\boldsymbol{M}^e+\beta\boldsymbol{K}_{\boldsymbol{u}}{}^e,$$

$$\boldsymbol{\Lambda}=\mathcal{A}_{e=1}^{n_{\text{elem}}}\boldsymbol{\Lambda}^e,\quad\boldsymbol{\Lambda}^e=\int_{\Omega^e}\left(\boldsymbol{B}_{\boldsymbol{u}}\right)^T\boldsymbol{\sigma}\,dV,$$

$$\boldsymbol{F}_{\boldsymbol{u}}=\mathcal{A}_{e=1}^{n_{\text{elem}}}\boldsymbol{F}_{\boldsymbol{u}}{}^e,\quad\boldsymbol{F}_{\boldsymbol{u}}{}^e=\int_{\Omega^e}(\boldsymbol{N}_{\boldsymbol{u}})^T\boldsymbol{b}\,dV+\int_{\Gamma_t}(\boldsymbol{N}_{\boldsymbol{u}})^T\boldsymbol{t}\,dS,$$

in which $\boldsymbol{\Lambda}(\boldsymbol{u},d)$ is the vector of internal forces, $\boldsymbol{K}_{\boldsymbol{u}}=\frac{\partial\boldsymbol{\Lambda}}{\partial\boldsymbol{u}}$, and $\boldsymbol{\sigma}$ denotes the Cauchy stresses in Voigt notation.

Modal damping ratios are typically calculated using the classical Rayleigh damping assumption, in which a linear combination of the mass and stiffness matrices defines the damping matrix $\mathbf{C}_d=\alpha\mathbf{M}+\beta\mathbf{K}_{\boldsymbol{u}}$. The natural frequencies of the structure are obtained by solving the eigenvalue problem $(\mathbf{K}_{\boldsymbol{u}}-\omega^2\mathbf{M})\boldsymbol{\phi}=\mathbf{0}$, where ω is the natural frequency and $\boldsymbol{\phi}$ is the mode shape (eigenvector). The modal damping ratio ζ_n for the n^{th} mode is then computed using the relation $\zeta_n=\frac{1}{2}\left(\frac{\alpha}{\omega_n}+\beta\omega_n\right)$.

Furthermore, the discretization of the crack evolution equation is expressed by the following equation:

$$\boldsymbol{R}_d(\boldsymbol{u},d)=\boldsymbol{K}_d\boldsymbol{d}-\boldsymbol{F}_d, \tag{12}$$

$$\boldsymbol{K}_d=\mathcal{A}_{e=1}^{n_{\text{elem}}}\boldsymbol{K}_d^e,\quad\boldsymbol{K}_d^e=\int_{\Omega^e}\left[\left(2\mathcal{H}+\frac{G_c}{\ell_0}\right)(\boldsymbol{N}_d)^T\boldsymbol{N}_d+G_c\ell_0(\boldsymbol{B}_d)^T\boldsymbol{B}_d\right]dV,$$

$$\boldsymbol{F}_d=\int_{\Omega^e}2\mathcal{H}(\boldsymbol{N}_d)^T\,dV.$$

2.3. Temporal discretization

In this study, the backward implicit (backward Euler) method is adopted due to its strong numerical stability and reliability in solving stiff and nonlinear problems. Compared to explicit methods such as forward Euler, which may diverge under certain conditions, the backward Euler scheme remains stable even with large time steps and provides robust convergence [41]. Moreover, its L-stability enables it to efficiently suppress rapid transients in a single time step, making it particularly useful when the goal is not to resolve fast dynamics in detail, but rather to damp them effectively without reducing the time step [42]. In contrast, the trapezoidal rule (Newmark's constant average acceleration scheme), although unconditionally stable and energy-conserving in linear dynamics, fails to eliminate initial transients effectively, causing oscillations to persist over multiple steps [42]. While it offers high accuracy among second-order implicit methods [43], it may become unstable in nonlinear analyses when large time steps are used [43,44]. Similarly, the generalized-α method, despite being designed to introduce algorithmic damping, may lead to undesired oscillations in the intermediate-frequency range and even converge to spurious high-energy solutions in some nonlinear regimes [44]. In the present work, both the generalized-α and Newmark methods were tested; however, convergence issues were encountered prior to crack propagation, likely due to the nonlinear stiffness introduced by damage localization. In contrast, the backward Euler method consistently converged, making it a more robust choice for the simulation of damage evolution.

The approximations of the velocity and acceleration at time step n are expressed by $\dot{\boldsymbol{u}}_n = \frac{\boldsymbol{u}_n - \boldsymbol{u}_{n-1}}{\Delta t}$, and $\ddot{\boldsymbol{u}}_n = \frac{\dot{\boldsymbol{u}}_n - \dot{\boldsymbol{u}}_{n-1}}{\Delta t} \rightarrow \ddot{\boldsymbol{u}}_n = \frac{\boldsymbol{u}_n - 2\boldsymbol{u}_{n-1} + \boldsymbol{u}_{n-2}}{\Delta t^2}$.

After substituting the above-mentioned expressions in Eq. (11),

$$\boldsymbol{R}_{\boldsymbol{u}}(\boldsymbol{u}, d) = \tilde{\boldsymbol{K}}_{\boldsymbol{u}} \boldsymbol{u}_n - \tilde{\boldsymbol{F}}_{\boldsymbol{u}} = \boldsymbol{0} \tag{13}$$

is solved to compute the displacements at time steps t^n where

$$\tilde{\boldsymbol{K}}_{\boldsymbol{u}} = \left(\frac{1}{\Delta t}\right)^2 \boldsymbol{M} + \left(\frac{1}{\Delta t}\right) \boldsymbol{C}_d + \boldsymbol{K}_{\boldsymbol{u}},$$

$$\tilde{\boldsymbol{F}}_{\boldsymbol{u}} = \boldsymbol{F}_{\boldsymbol{u}} + \boldsymbol{M}\left(\frac{1}{\Delta t}\right)^2 [2\boldsymbol{u}_{n-1} - \boldsymbol{u}_{n-2}] + \left(\frac{1}{\Delta t}\right) \boldsymbol{C}_d \boldsymbol{u}_{n-1}.$$

Furthermore $\boldsymbol{K}_{\boldsymbol{u}} = \frac{\partial \boldsymbol{\Lambda}(\boldsymbol{u}_n, d_n)}{\partial \boldsymbol{u}_n} = \mathcal{A}_{e=1}^{n_{\text{elem}}} \boldsymbol{K}_{\boldsymbol{u}}^e(\boldsymbol{u}_n, d_n)$, $\boldsymbol{K}_{\boldsymbol{u}}^e(\boldsymbol{u}_n, d_n) = \int_{\Omega^e} \left(\boldsymbol{B}_{\boldsymbol{u}}\right)^T \boldsymbol{C}(\boldsymbol{u}_n, d_n)\, \boldsymbol{B}_{\boldsymbol{u}}\, dV$, and $\boldsymbol{C}$ represents the elasticity tensor $C = \frac{\partial^2 \psi}{\partial \epsilon^2} = \frac{\partial^2}{\partial \epsilon^2}\left(g(d)\psi_0^+(\boldsymbol{\varepsilon}) + \psi_0^-(\boldsymbol{\varepsilon})\right) = g(d)\frac{\partial^2 \psi_0^+(\boldsymbol{\varepsilon})}{\partial \epsilon^2} + \frac{\partial^2 \psi_0^-(\boldsymbol{\varepsilon})}{\partial \epsilon^2}$ in Voigt notation.

In the monolithic approach, the Newton–Raphson algorithm can be utilized to solve the coupled system of governing equations iteratively, as expressed follows:

$$-\boldsymbol{R} = \begin{bmatrix} -\boldsymbol{R}_{\boldsymbol{u}}(\boldsymbol{u}_n^k, \boldsymbol{d}_n^k) \\ -\boldsymbol{R}_d(\boldsymbol{u}_n^k, \boldsymbol{d}_n^k) \end{bmatrix} = \begin{bmatrix} \boldsymbol{K}_{\boldsymbol{uu}}(\boldsymbol{u}_n^k, \boldsymbol{d}_n^k) & \boldsymbol{K}_{\boldsymbol{ud}}(\boldsymbol{u}_n^k, \boldsymbol{d}_n^k) \\ \boldsymbol{K}_{d\boldsymbol{u}}(\boldsymbol{u}_n^k, \boldsymbol{d}_n^k) & \boldsymbol{K}_{dd}(\boldsymbol{u}_n^k, \boldsymbol{d}_n^k) \end{bmatrix} \begin{bmatrix} \Delta \boldsymbol{u}^k \\ \Delta \boldsymbol{d}^k \end{bmatrix}, \quad \boldsymbol{K}_{\alpha\beta} = \frac{\partial \boldsymbol{R}_\alpha}{\partial \beta}, \quad \alpha, \beta \in \{\boldsymbol{u}, d\}, \tag{14}$$

The displacement and phase-field variables at the n^{th} time step and $k+1^{\text{th}}$ iteration are computed as $\boldsymbol{u}_n^{k+1} = \boldsymbol{u}_n^k + \Delta \boldsymbol{u}_n^k$ and $\boldsymbol{d}_n^{k+1} = \boldsymbol{d}_n^k + \Delta \boldsymbol{d}_n^k$.

The non-convex nature of the functional (1) often causes the Newton–Raphson iterations to diverge, particularly during abrupt crack propagation and in the post-peak loading regime. However, Eq. (1) remains convex with respect to each variable individually. Therefore, the equations can be solved using an alternating approach, where one variable is fixed while the other is updated, and this process is repeated iteratively [45]. Consequently, the coupled equations (12) and (13) can be solved using the staggered scheme as follows:

$$-\boldsymbol{R} = \begin{bmatrix} -\boldsymbol{R}_{\boldsymbol{u}}(\boldsymbol{u}_n^k, \boldsymbol{d}_n^k) \\ -\boldsymbol{R}_d(\boldsymbol{u}_n^k, \boldsymbol{d}_n^k) \end{bmatrix} = \begin{bmatrix} \boldsymbol{K}_{\boldsymbol{uu}}(\boldsymbol{u}_n^k, \boldsymbol{d}_n^k) & \boldsymbol{0} \\ \boldsymbol{0} & \boldsymbol{K}_{dd}(\boldsymbol{u}_n^k, \boldsymbol{d}_n^k) \end{bmatrix} \begin{bmatrix} \Delta \boldsymbol{u}^k \\ \Delta \boldsymbol{d}^k \end{bmatrix}, \tag{15}$$

It is noteworthy that equation (15) differs from the staggered equations of Miehe's method [19]:

$$-\boldsymbol{R} = \begin{bmatrix} -\boldsymbol{R}_{\boldsymbol{u}}(\boldsymbol{u}_n^k, \boldsymbol{d}_n^{k+1}) \\ -\boldsymbol{R}_d(\boldsymbol{u}_n^k, \boldsymbol{d}_n^k) \end{bmatrix} = \begin{bmatrix} \boldsymbol{K}_{\boldsymbol{uu}}(\boldsymbol{u}_n^k, \boldsymbol{d}_n^{k+1}) & \boldsymbol{0} \\ \boldsymbol{0} & \boldsymbol{K}_{dd}(\boldsymbol{u}_n^k, \boldsymbol{d}_n^k) \end{bmatrix} \begin{bmatrix} \Delta \boldsymbol{u}^k \\ \Delta \boldsymbol{d}^k \end{bmatrix}, \tag{16}$$

and from Molnár's method [46]:

$$-\boldsymbol{R} = \begin{bmatrix} -\boldsymbol{R}_{\boldsymbol{u}}(\boldsymbol{u}_n^k, \boldsymbol{d}_n^{k=0}) \\ -\boldsymbol{R}_d(\boldsymbol{u}_n^{k=0}, \boldsymbol{d}_n^k) \end{bmatrix} = \begin{bmatrix} \boldsymbol{K}_{\boldsymbol{uu}}(\boldsymbol{u}_n^k, \boldsymbol{d}_n^{k=0}) & \boldsymbol{0} \\ \boldsymbol{0} & \boldsymbol{K}_{dd}(\boldsymbol{u}_n^{k=0}, \boldsymbol{d}_n^k) \end{bmatrix} \begin{bmatrix} \Delta \boldsymbol{u}^k \\ \Delta \boldsymbol{d}^k \end{bmatrix}. \tag{17}$$

As reported by several references [45,47,48], Miehe's staggered method has a very low convergence rate. In dynamic simulations, staggered schemes may require more iterations to achieve convergence than in quasi-static cases because of the higher complexity of the problem. On the other hand, Molnár's staggered method exhibits very good convergence [46]. However, our evaluations indicate that, although Molnár's method produces results comparable to Miehe's method for certain static problems, it can significantly affect the accuracy in dynamic problems, since the displacement variable is frozen in the phase-field equation and the phase variable is frozen in the equilibrium equation at each step. In contrast, the analyses presented in Section 4 demonstrate that the method proposed in Eq. (15) not only exhibits a reasonable convergence rate, but also improves accuracy by consistently accounting for the influence of both the displacement and phase variables on both the equilibrium and phase-field equations throughout each step.

3. Mesh-adaptive refinement strategy

In the simulation of crack propagation, achieving high accuracy demands a mesh with fine discretization near the crack. However, using a uniformly fine mesh for the entire domain yields extremely high computational costs. A more efficient approach is to first perform a preliminary analysis using a coarse mesh and then apply an adaptive strategy to refine the mesh only in critical regions, particularly around the crack. In this study, we propose a multi-level gradually adaptive mesh refinement method to tackle fracture problems using the phase-field approach. One of the critical challenges in adaptive mesh refinement techniques is to determine appropriate refinement criteria that define both the location and the level of refinement. In the phase-field method, the location of refinement can be determined automatically due to the fact that fracture is an intrinsic feature of the problem and progresses naturally within the domain. To refine the mesh in regions where the crack propagates, the allowable distance between field nodes can be determined based on the phase-field variable. This means that the refinement level is directly related to the extent of damage. It is assumed that the field nodes of each element are evenly distributed on a circle around its center. The circumferential distance between field nodes within an element can be approximated as follows:

$$L_i = \frac{2 \times \pi \times r^i_{\text{mean}}}{n'} \tag{18}$$

where r^i_{mean} represents the mean radius of the i^{th} element and n' the total number of field nodes associated with the respective element. As an illustrative example, the method for calculating the circumferential distance of a 6-node element is depicted in Fig. 2.

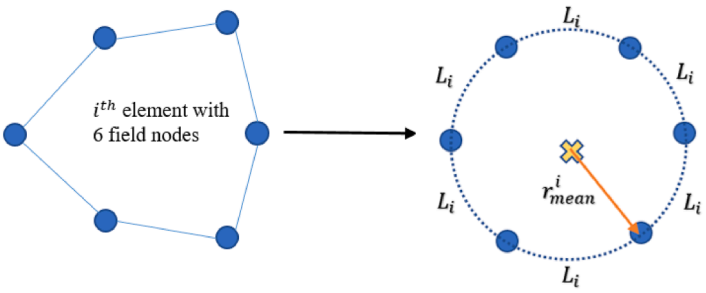

Fig. 2. Element nodes uniformly distributed on the circle's perimeter.

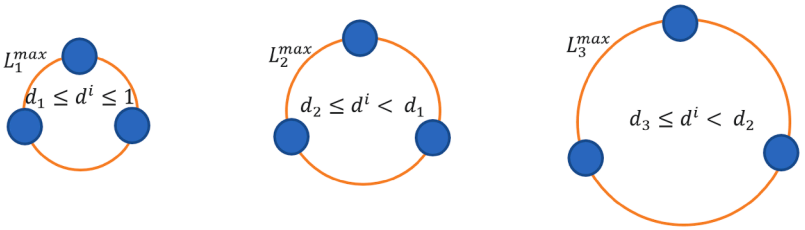

Fig. 3. A schematic of the maximum distance between field nodes as a function of the damage level. It is assumed that the field nodes of each element are distributed on the circle's perimeter around its center point.

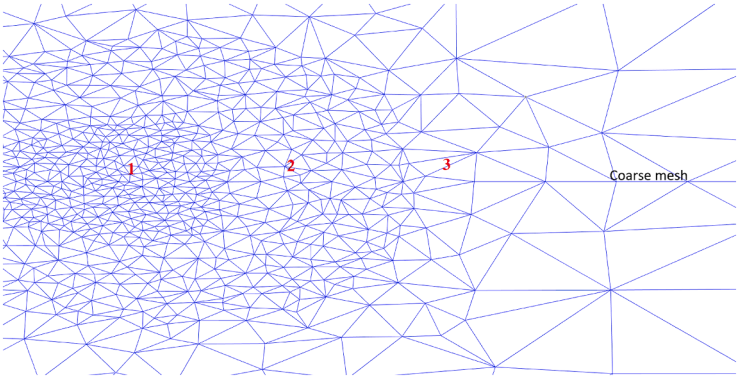

Fig. 4. An example of three levels of mesh refinement.

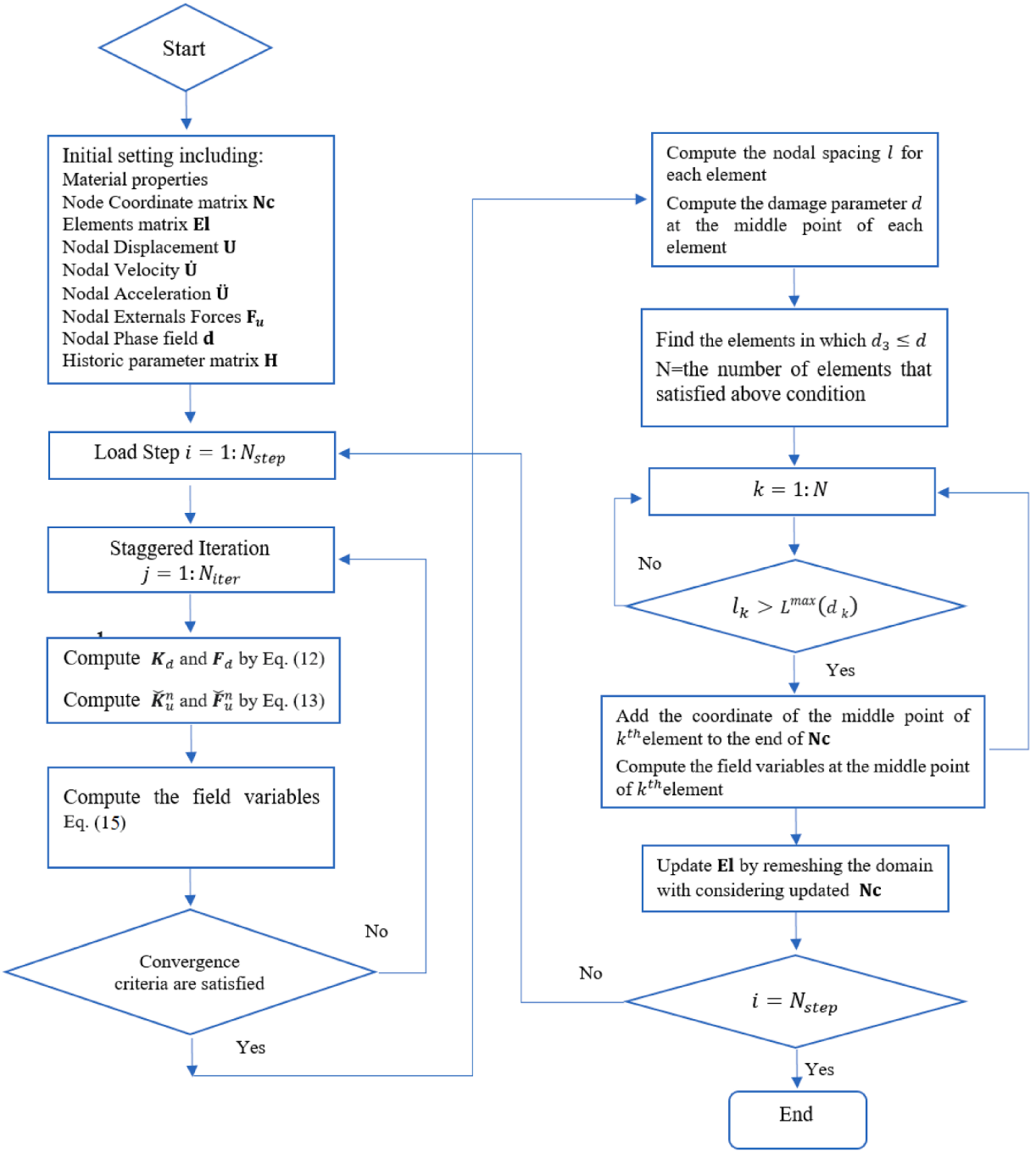

Fig. 5. Flowchart of proposed method.

Based on this definition, a multi-level gradually adaptive mesh refinement strategy can be easily established. Now, different refinement levels can be assigned based on the phase-field parameter. At each level, the mesh is progressively refined in regions where fracture evolution is occurring, ensuring a balance between computational efficiency and accuracy. This hierarchical refinement strategy enables efficient modeling of fracture propagation while minimizing unnecessary computational costs in less critical areas. For instance, in a three-level refinement approach as shown in Fig. 3, the maximum allowable distance between field nodes is defined as follows:

$$L^{\max}(d^i) = \begin{cases} L_1^{\max} & \text{for } d_1 \leq d^i \leq 1 \\ L_2^{\max} & \text{for } d_2 \leq d^i < d_1 \\ L_3^{\max} & \text{for } d_3 \leq d^i < d_2 \end{cases}, \qquad \begin{matrix} d_1 \geq d_2 \geq d_3 \\ L_1^{\max} \leq L_2^{\max} \leq L_3^{\max} \end{matrix} \tag{19}$$

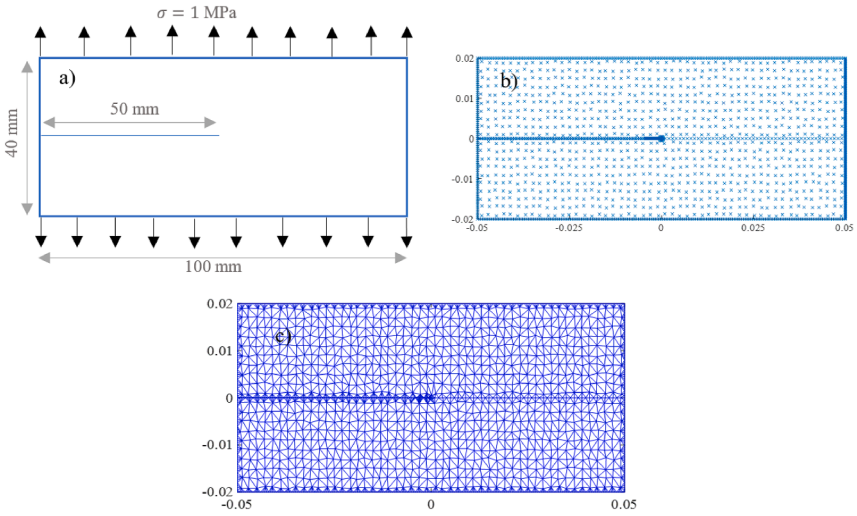

Fig. 6. a) The geometry and boundary conditions, b) Initial field nodes, c) Initial mesh with three-noded elements.

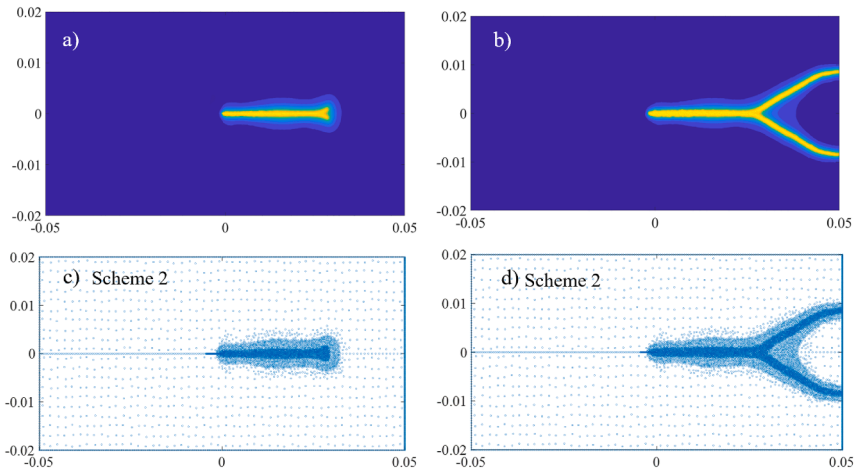

Fig. 7. Crack propagation in material without damping at different time steps (1000, 1560) along with corresponding field nodes (single notched plate).

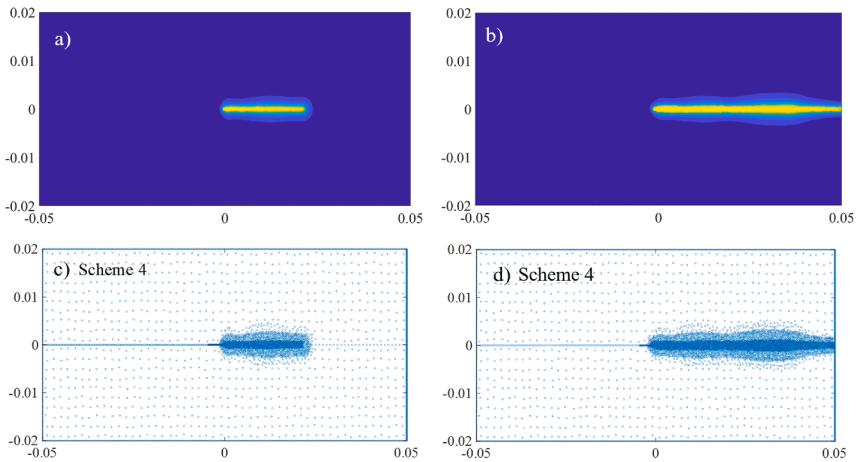

Fig. 8. Crack propagation in material with damping at different time steps (900, 1650) along with corresponding field nodes (single notched plate).

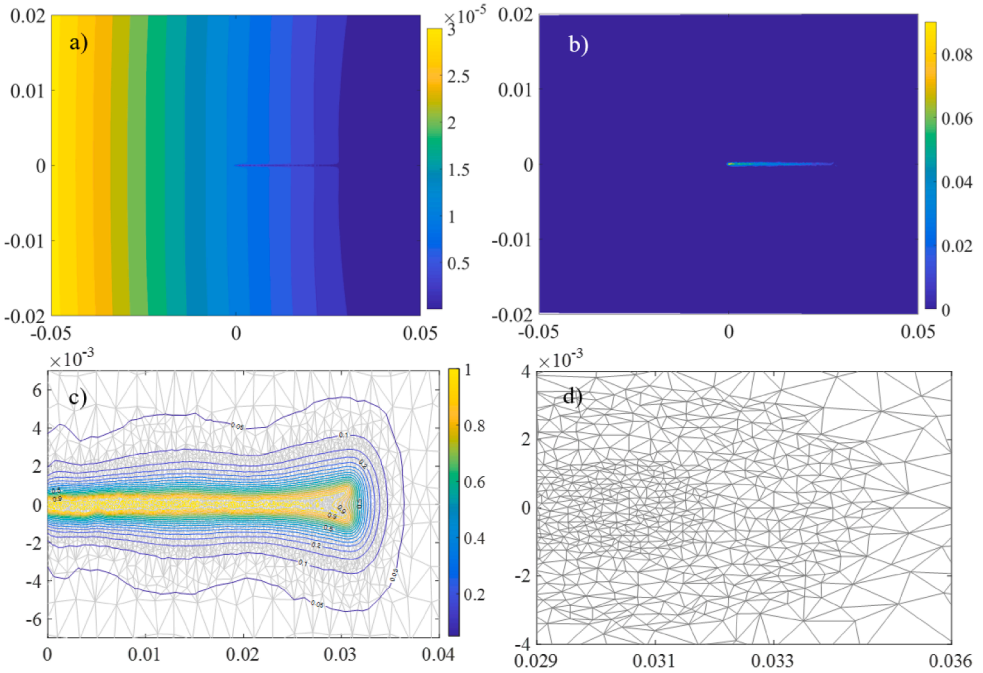

Fig. 9. a) $|u_y|$, b) ϵ_y, c) phase-field variable, and d) crack tip elements for scheme 5 at $t = 54$ μs (single notched plate).

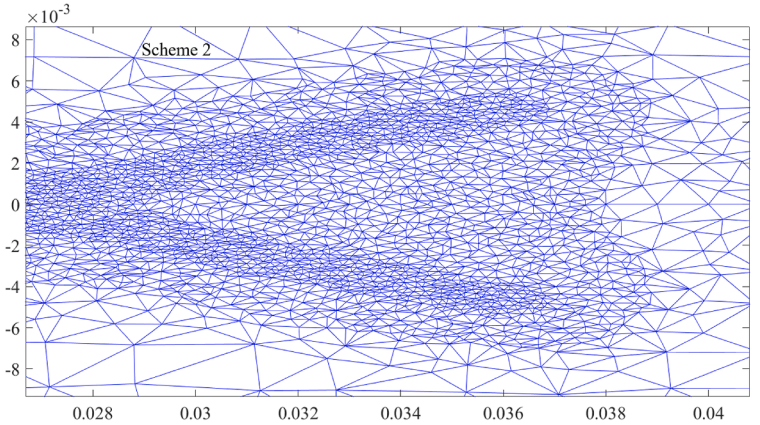

Fig. 10. Elements located at the crack tip (single notched plate).

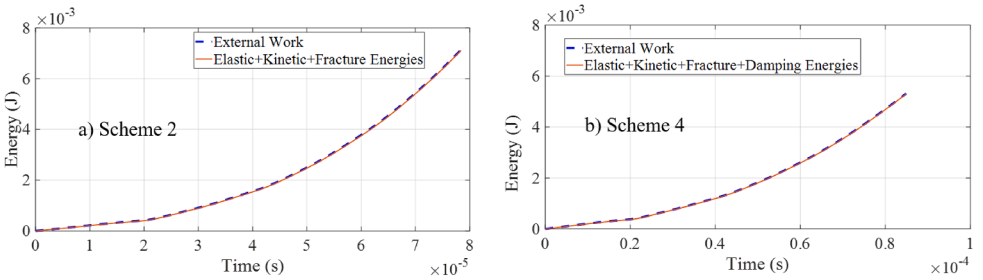

Fig. 11. Comparison between external work and summation of other energies (single notched plate).

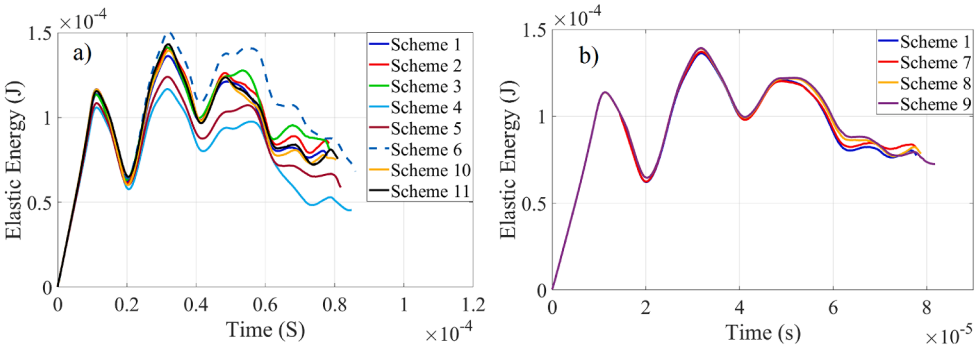

Fig. 12. Elastic energies for different schemes (single notched plate).

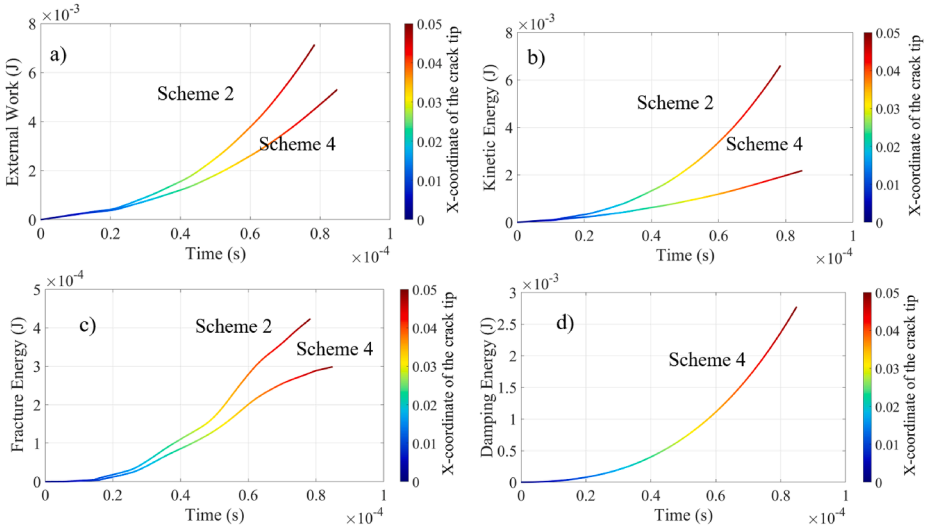

Fig. 13. Energy responses (single notched plate).

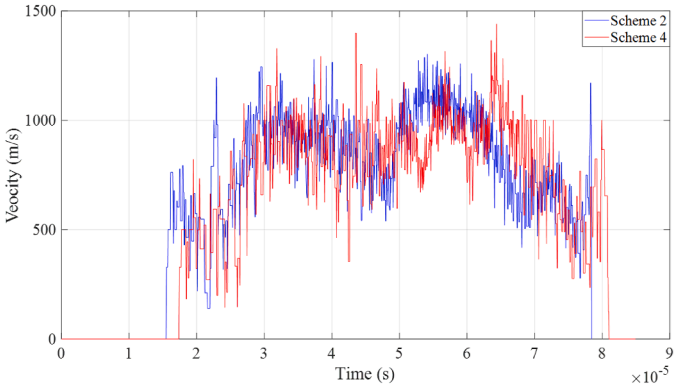

Fig. 14. Crack velocity with and without damping (single notched plate).

where $L^{\max}$ represent the maximum circumferential nodal spacing corresponding to damage levels d^i. The phase-field variable d^i is evaluated at the midpoint of each element. The damage parameter is determined through the crack evolution equation. To define the nodal spacing, the maximum allowable distance between nodes in the domain can be chosen as half of the phase-field length scale ℓ_0, as suggested in [19]. In intact regions, the mesh size is maintained at a predefined coarse level. In other regions, the mesh is refined gradually across multiple levels according to the extent of damage. To ensure a proper nodal distribution in the damaged zones, a new field node is introduced at the midpoint of an element whenever the nodal spacing exceeds the specified threshold.

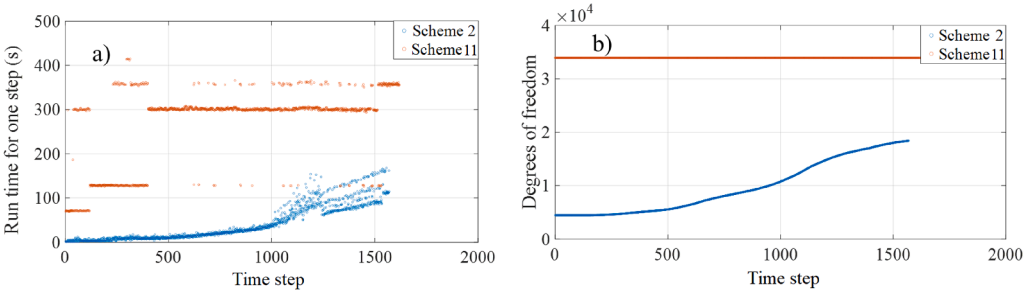

Fig. 15. Comparison of a) runtime and b) number of degrees of freedom in each step for mesh-adaptive and fixed mesh schemes (single notched plate).

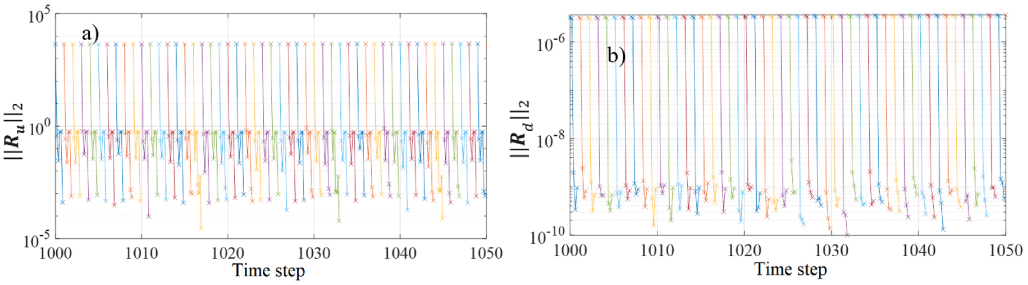

Fig. 16. Convergence patterns (single notched plate).

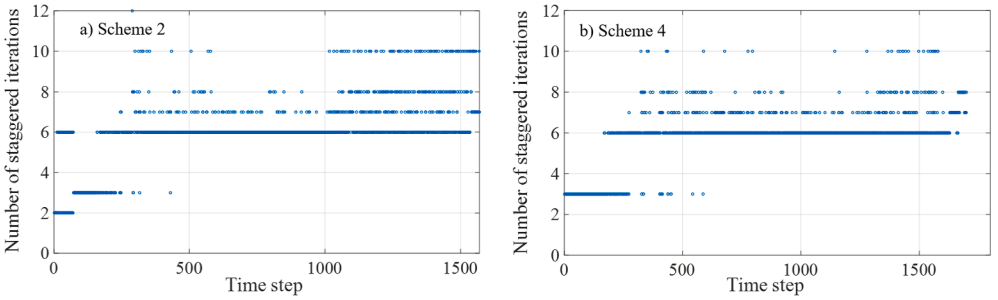

Fig. 17. Number of staggered iterations (single notched plate).

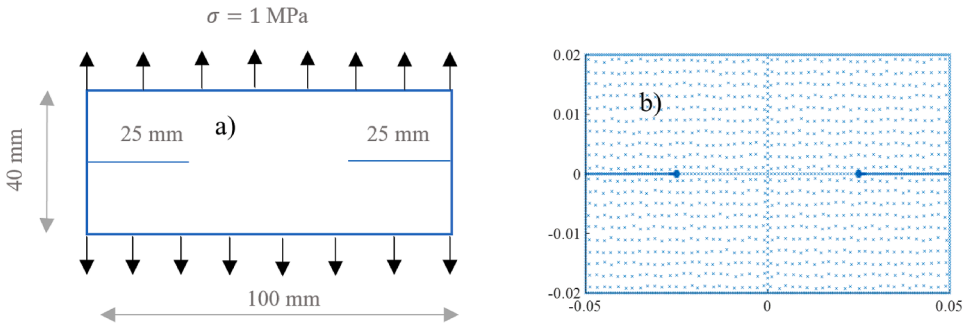

Fig. 18. a) The geometry and boundary conditions, b) Initial field nodes.

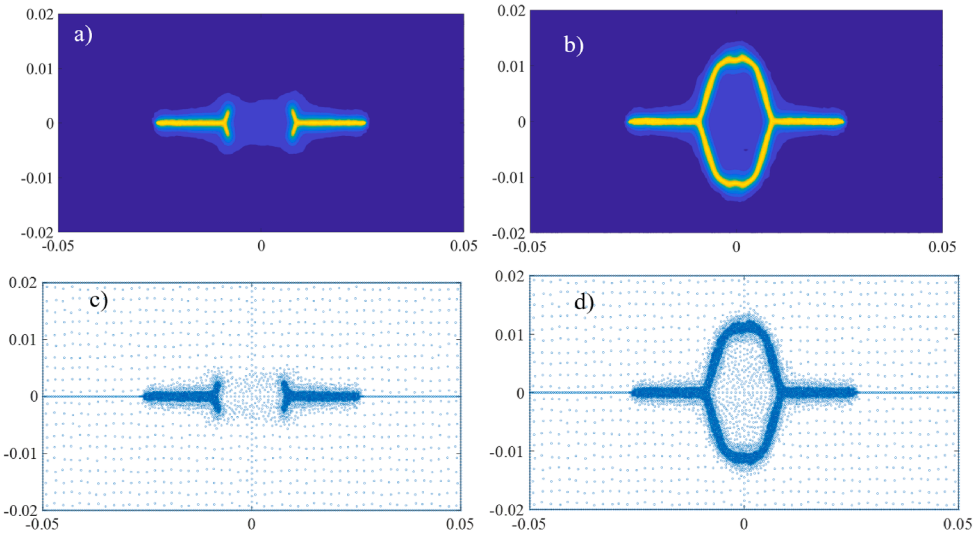

Fig. 19. Crack propagation in material without damping at different time steps (1750, 2300) along with corresponding field nodes (double notched plate).

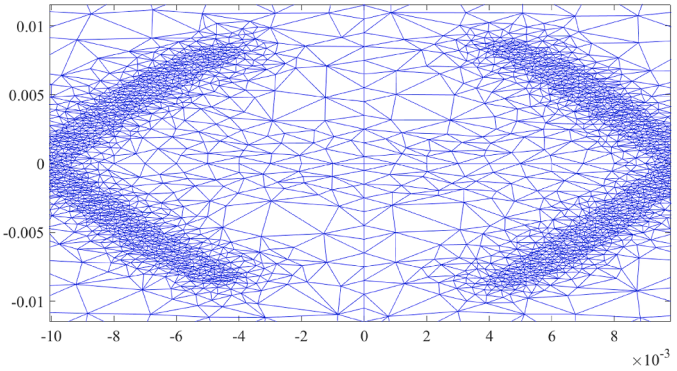

Fig. 20. Elements located at the crack tip (double notched plate).

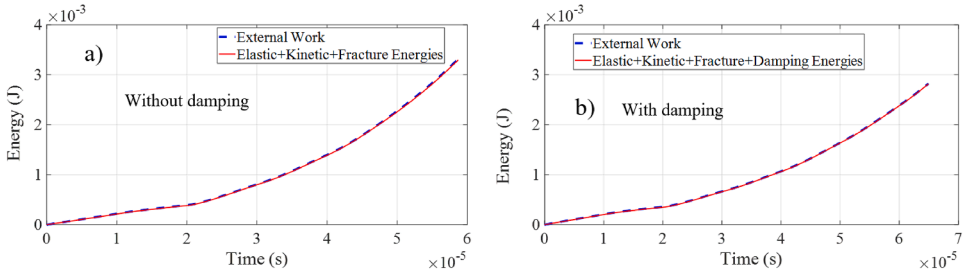

Fig. 21. Comparison between external work and summation of other energies (double notched plate).

For efficiency, field nodes are inserted only into the refinement region, while those on the boundaries remain fixed. Once the new field nodes are introduced, the entire domain is re-meshed accordingly. The updated mesh is subsequently used to compute the field variables, such as displacement and phase-field values, at the newly introduced nodes. Since mesh refinement introduces only new nodes without altering the positions of existing ones, the unknown variables (displacement and phase-field values) at the existing nodes are directly transferred from the old mesh to the new one. For the newly added nodes, the unknown variables are estimated by interpolating the values of neighboring nodes, which, in this study, is performed by averaging the surrounding nodal values. Therefore, since the unknown variables on the new mesh can be obtained rapidly, the associated computational cost of transferring

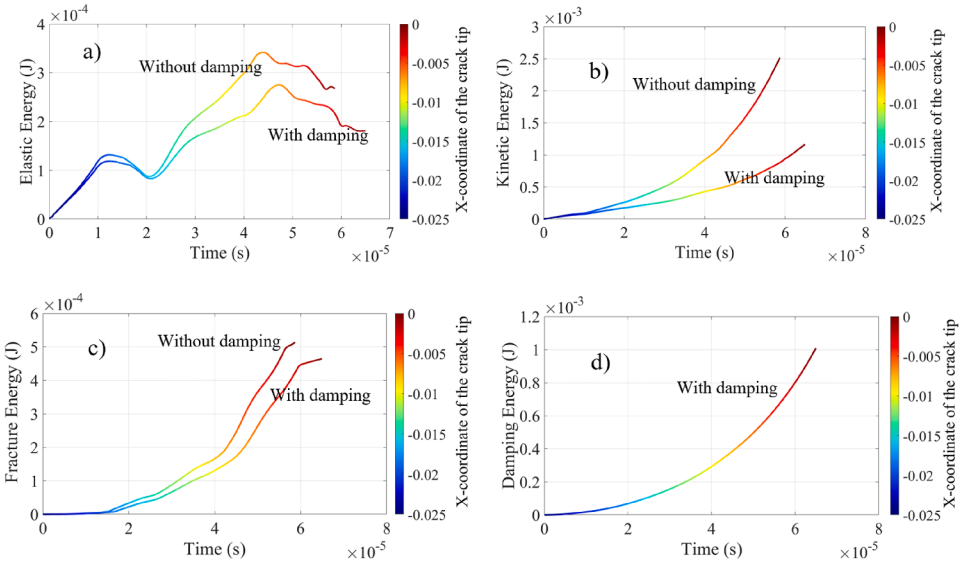

Fig. 22. Energy responses (double notched plate).

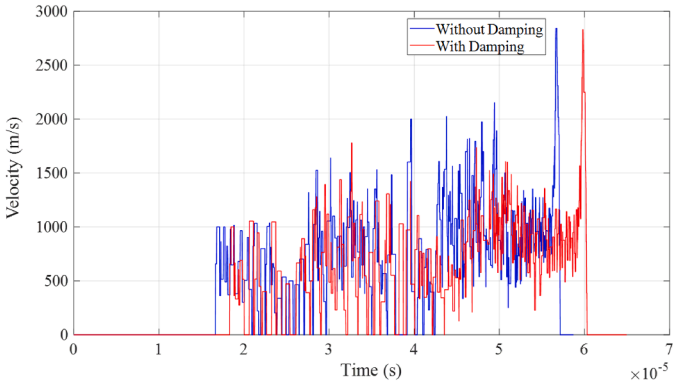

Fig. 23. Crack velocity (double notched plate).

data during mesh refinement is negligible. A representative example of three-level mesh refinement and the corresponding flowchart are presented in Figs. 4 and 5, respectively. The computational code was implemented in MATLAB. In our implementation, the history field, evaluated at Gauss points rather than nodal points, is interpolated between refined and coarsened elements using MATLAB's standard interpolation function scatteredInterpolant, which employs a Delaunay triangulation-based linear interpolation scheme.

4. Numerical simulation

This section discusses the performance of the proposed method on various 2D problems. The first example is a dynamic crack propagation problem, as considered by Ref[49]. The second example involves dynamic crack branching in a double-notched plate. Finally, the last example examines crack propagation in the dynamic Kalthoff test. Linear three-noded triangular finite elements are employed in all the examples presented.

The time step size was selected following the guideline $\Delta t = h/v_R$ to achieve accurate results, as suggested by Borden et al. [24] , where h is the element size and v_R is the Rayleigh wave speed in the material. For the first example, time steps of 1×10^{-7} s and 5×10^{-8} s were used, while for the second example, which is geometrically similar but features a different notch configuration, the time step was further reduced to 2.5×10^{-8} s to ensure accuracy. For the third example, an even smaller time step of 1×10^{-8} s was adopted, compared with 1.25×10^{-8} s reported by Borden et al. [24]. No viscous damping term was included in the phase-field equation, in accordance with the aforementioned reference.

In nonlinear time-history analyses, the use of the classical Rayleigh damping model, composed of mass-proportional and stiffness-proportional components, has been shown to cause both physical and numerical problems when the stiffness-proportional term is included. As discussed by Hall [50], when the damping matrix is based on the initial elastic stiffness, a reduction of structural stiffness during softening or yielding phases may lead to unrealistically large damping forces compared to the actual restoring forces. This

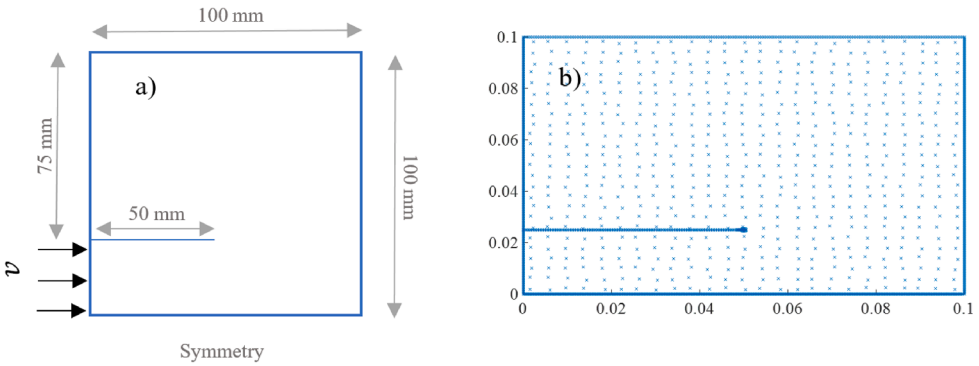

Fig. 24. a) Geometry and boundary conditions, b) Initial field nodes.

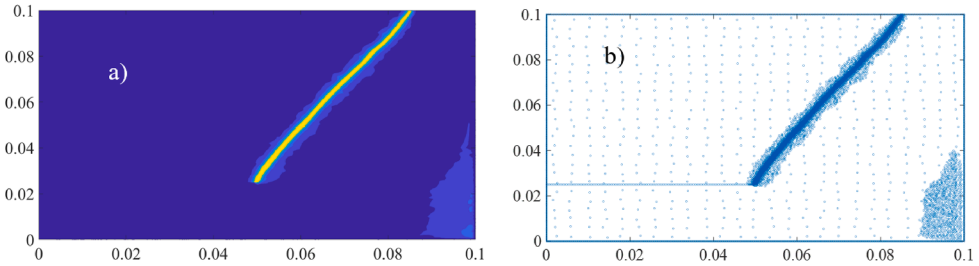

Fig. 25. Crack propagating in material without damping at final time step along with corresponding field nodes (Kalthoff test).

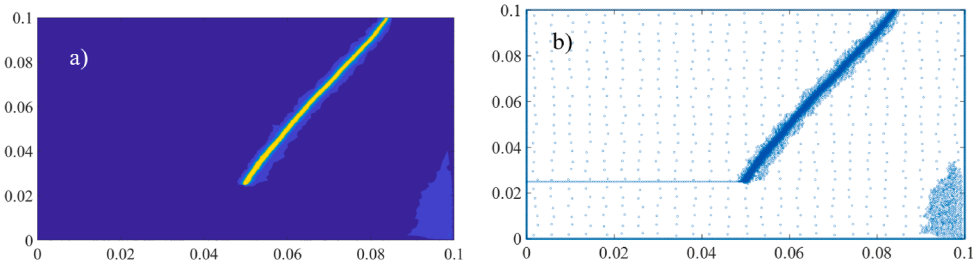

Fig. 26. Crack propagating in material with damping at final time steps along with corresponding field nodes (Kalthoff test).

artificial amplification of damping forces can result in a non-conservative energy dissipation behavior. Moreover, Jehel et al. [51] observed that when the tangent stiffness matrix is used, the continuous update of stiffness throughout the inelastic analysis can cause convergence difficulties in solution algorithms. In our implementation, when the tangent stiffness-proportional term of Rayleigh damping was considered, the tangent stiffness matrix to compute the damping matrix was frozen after several iterations in each step. This treatment stabilized the solution process and ensured numerical convergence. However, we observed pronounced spatial gradients of damping forces within the domain, particularly in the vicinity of cracks. In addition, an increase in elastic strain energy compared with the undamped case was noted, which may suggest artificial energy input possibly arising from nonphysical damping effects. To eliminate such undesirable behavior, the stiffness-proportional term was therefore omitted in the present study, and only the mass-proportional component of Rayleigh damping was retained.

It is noticeable that the inclusion of Rayleigh damping incurs negligible computational cost per iteration, as it relies on the already computed stiffness and mass matrices. The increased total run time that may be observed in the damping case is mainly due to the reduced average crack propagation velocity, which requires a greater number of time steps to complete the fracture process. All computations were performed using MATLAB on a workstation equipped with an AMD Ryzen 9 7950X processor (4.0–5.88 GHz) and 64 GB of RAM. The reported computational time corresponds to the wall-clock time.

4.1. Dynamic crack branching in a single-notched plate

In this example, we simulate a pre-notched rectangular plate subjected to dynamic tensile loading. The geometry and boundary conditions are illustrated in Fig. 6a. The traction load applied to the top and bottom surfaces at the start of the simulation remains constant throughout. All other surfaces have zero traction. Under this loading condition, crack branching is expected to occur. The

Table 1
Parameters of different schemes.

Scheme	Time step (μs)	Length scale l_0 (m)	Damping parameter α (s^{-1})	d_1	d_2	d_3	Initial number of elements	Final number of elements	Total runtime	Staggered method
1	0.1	5×10^{-4}	0	0.5	0.1	0.05	3,296	16,704	8 h 53 min	Eq. (15)
2	0.05	5×10^{-4}	0	0.5	0.1	0.05	3,296	17,246	17 h 46 min	Eq. (15)
3	0.1	2.5×10^{-4}	0	0.5	0.1	0.05	3,296	30,656	41 h 40 min	Eq. (15)
4	0.05	5×10^{-4}	2×10^{4}	0.5	0.1	0.05	3,296	12,870	10 h 16 min	Eq. (15)
5	0.1	5×10^{-4}	1×10^{4}	0.5	0.1	0.05	3,296	15,568	8 h 46 min	Eq. (15)
6	0.05	5×10^{-4}	0	0.5	0.1	0.05	3,296	19,382	11 h 5 min	Eq. (17)
7	0.1	5×10^{-4}	0	0.5	0.2	0.05	3,296	14,690	6 h 17 min	Eq. (15)
8	0.1	5×10^{-4}	0	0.7	0.1	0.05	3,296	15,580	8 h 1 min	Eq. (15)
9	0.1	5×10^{-4}	0	0.7	0.2	0.05	3,296	13,560	6 h 41 min	Eq. (15)
10	0.05	5×10^{-4}	0	All nodal spaces ($L_{i=1:3}^{\max}$) are reduced by 80 %			4,646	26,106	30 h 33 min	Eq. (15)
11	0.05	5×10^{-4}	0	Fixed mesh with 2.5×10^{-4} nodal spacing in the expected crack propagation region			32,422	32,422	122 h 13 min	Eq. (15)

model parameters are set as follows: density $\rho = 2450\,\mathrm{kg\,m^{-3}}$, Young's modulus $E = 32\,\mathrm{GPa}$, Poisson's ratio $\nu = 0.2$, thickness $t = 1\,\mathrm{mm}$ and fracture toughness $G_c = 3\,\mathrm{J\,m^{-2}}$. Plane strain conditions are assumed.

To calculate the natural frequencies of the problem, the top and bottom edges of the plate are fixed. The first natural frequency is obtained by solving the generalized eigenvalue problem, yielding a result of $\omega = 1.73 \times 10^5\,\mathrm{rad\,s^{-1}}$. Assuming Rayleigh damping with $\beta = 0$, the damping matrix is calculated as $C_d = \alpha M$, $\alpha = 2\xi_1\omega_1$. Assuming damping ratios of 3 % and 6 % the coefficient α is taken approximately as $1 \times 10^4\,\mathrm{s^{-1}}$ and $2 \times 10^4\,\mathrm{s^{-1}}$, respectively. This value is assumed to remain constant throughout the analysis. The other parameters for adaptive mesh refinement are $L_1^{\max} = 0.7\ell_0$, $L_2^{\max} = 1.2\ell_0$ and $L_3^{\max} = 3\ell_0$. According to Table 1, 11 different schemes are considered to solve this problem.

Figs. 7 and 8 illustrate the crack path without and with damping, respectively, along with the corresponding field nodes at different time steps.

The distributions of displacement and strain in the y-direction, as well as the phase-field variable and the associated finite elements, are depicted in Figure 9.

Fig. 10 shows the crack tip elements after approximately half of the crack has propagated. It can be observed that the elements around the crack have progressively been refined in a systematic manner across three levels.

Numerical instabilities can lead to artificial energy generation, thereby violating energy conservation. Hence, verifying energy balance provides a practical means to assess the stability of nonlinear computations [52]. A comparison between the external work and the sum of elastic, kinetic, fracture, and (if considered) damping energies is presented in Fig. 11. As can be seen, the external work closely matches the sum of the other energies.

Fig. 12 shows the elastic energies for different schemes. It can be observed that by including damping, the elastic energy in the structure is significantly reduced. Additionally, the time required for the crack to fully propagate is increased. Moreover, the results of Scheme 10, which employs adaptive meshing, are very close to those of Scheme 11, which uses a conventional finite element method with a locally pre-refined mesh in the expected crack propagation region. According to Table 1, the computational time for Scheme 10 is 30.5 h, compared to 122.2 h for Scheme 11. Moreover, Scheme 6, which follows the staggered approach of Eq. (17), i.e., Molnár's method [46], exhibits a significant error due to freezing the variables at each step. In Molnár's method [46], each time step typically converges within 4 iterations, with an approximate total computation time of 11 h. In contrast, for Miehe's staggered scheme [19], the convergence rate significantly reduces after step 870, and even with 20 iterations per step, the solutions fail to converge. Moreover, the sensitivity of the results to the adaptive mesh parameters (d_1 and d_2) has been investigated in Figure 12b, showing that a rational choice of these parameters yields acceptable results, and the variations between the outcomes are insignificant.

Fig. 13 shows the curves comparing the external work, the kinetic energy, and the energy dissipated by crack propagation and damping. The external work energy in the damping case is lower than in the non-damping case, indicating that the average displacement at the top and bottom boundaries has decreased in the presence of damping. Additionally, the reduction in energy dissipated by crack propagation in the damping case can be attributed to both the shorter crack length and the absence of crack branching, compared to the non-damping case. The comparison of kinetic energies in the damping and non-damping cases (Schemes 4 and 2), reveals that the damping has had a significant impact on this energy, reducing it by approximately one third. The crack propagation velocity is shown in Fig. 14. Generally, damping increases the time required for the crack to fully propagate.

Fig. 15 a) presents a comparison of the runtime in each step for Scheme 2 and Scheme 11, corresponding to the adaptive mesh and fixed mesh approaches, respectively. It is observed that up to step 500, the runtime at each step for the adaptive mesh is negligible. However, as the number of field nodes increases, the runtime increases as well. The noticeable fluctuations in runtime between adjacent steps are attributed to the varying number of iterations required for convergence in each step. Additionally, the evolution of the degrees of freedom at each step is illustrated in Fig. 15 b).

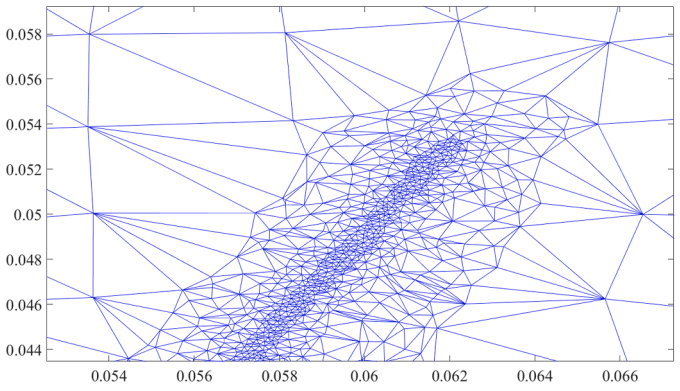

Fig. 27. Crack tip's elements (Kalthoff test).

The convergence behavior and the reduction of the 2-norm of the residuals between steps 1000 and 1050 are shown in Fig. 16. The residual of the mechanical problem $\|\boldsymbol{R}_u\|_2$ typically decreases from 1e4 to 1e-3 within 6 iterations, while the residual of the phase-field problem $\|\boldsymbol{R}_d\|_2$ reaches 1e-9. The number of staggered iterations for Schemes 2 and 4 are presented in Fig. 17.

4.2. Dynamic crack branching in a double-notched plate

In the second example, we evaluate the proposed method using a rectangular double-notched plate, as shown in Fig. 18. The time step size is $\Delta t_1 = 0.025\,\mu s$ and the same material parameters as in the previous example are applied. The parameters for adaptive mesh refinement are $L_1^{\max} = 0.7\ell_0$, $L_2^{\max} = 1.5\ell_0$, $L_3^{\max} = 3\ell_0$, $d_1 = 0.5$, $d_2 = 0.2$, and $d_3 = 0.1$.

Fig. 19 illustrates the crack evolution and the corresponding field nodes. Since the crack growth paths in the damped and undamped cases are similar, only one case is reported. The cracks initiate at the end of the notches, then propagate through the matrix, eventually forming complex branching patterns. The results also demonstrate that the proposed model effectively refines the mesh in regions where crack propagation is expected.

The element refinement around the crack is shown in Fig. 20, where the elements are reduced in size in three stages, transitioning from intact material to complete failure.

Fig. 21 shows a comparison between the external work and the sum of elastic, kinetic, fracture, and (if considered) damping energies. The close agreement between these two curves demonstrates the stability of nonlinear computations.

The energy responses are shown in Fig. 22. It can be observed that, given the constant external force, the elastic and kinetic energies are reduced in the damped case compared to the undamped ones. This reduction can be attributed to the decrease in displacements and velocities at the nodes due to the presence of damping. As seen in Fig. 23, considering damping reduces the average crack growth rate.

4.3. Dynamic Kalthoff test

In this example, the classic Kalthoff experiment is analyzed, where a specimen with symmetric pre-notches is impacted by a rapidly moving projectile. A schematic representation of the geometry and boundary conditions is shown in Fig. 24. The applied velocity boundary condition is defined as follows:

$$v = \begin{cases} \dfrac{t}{t_0}\, v_0 & t \le t_0 \\ v_0 & t > t_0 \end{cases}$$

where $v_0 = 16.5\,\mathrm{m\,s^{-1}}$ and $t_0 = 1\,\mu s$. The material parameters are set as follows: density $\rho = 8000\,\mathrm{kg\,m^{-3}}$, Young's modulus $E = 190\,\mathrm{GPa}$, Poisson's ratio $\nu = 0.3$, and fracture toughness $G_c = 2.213 \times 10^4\,\mathrm{J\,m^{-2}}$. The length scale and time step size are considered as $\ell_0 = 3.9 \times 10^{-1}\,\mathrm{mm}$ and $\Delta t = 0.01\,\mu s$. Plane strain conditions are assumed. The parameters for adaptive mesh refinement are $L_1^{\max} = 0.7\ell_0$, $L_2^{\max} = 1.5\ell_0$, $L_3^{\max} = 3\ell_0$, $d_1 = 0.5$, $d_2 = 0.2$, and $d_3 = 0.1$.

The crack growth paths in the undamped and damped cases along with the field nodes are shown in Figs. 25 and 26, respectively. The crack growth angle in the undamped and damped cases is approximately 65.7° and 66.4°, respectively, which is close to the experimental result of 70°. Moreover, the crack tip elements are depicted in Fig. 27.

As seen in Fig. 28, the external work and the sum of elastic, kinetic, fracture, and (if considered) damping energies are also very close to each other in this example. Moreover, damping has increased the level of external force, which is reflected in the increase in external work. The energy responses are presented in Fig. 29. Damping reduces the nodal velocities, leading to a decrease in kinetic energy. On the other hand, damping increases the level of elastic energy.

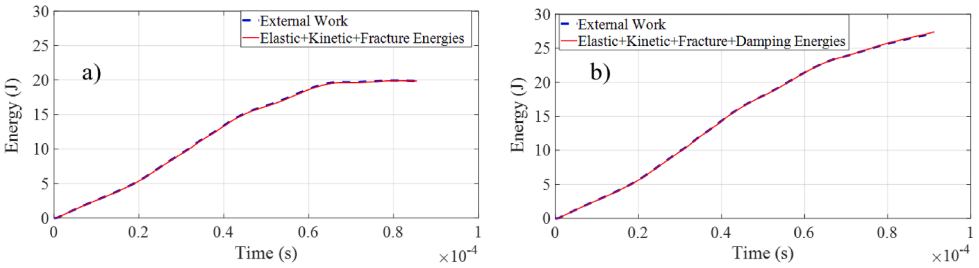

Fig. 28. Comparison between external work and summation of other energies (Kalthoff test).

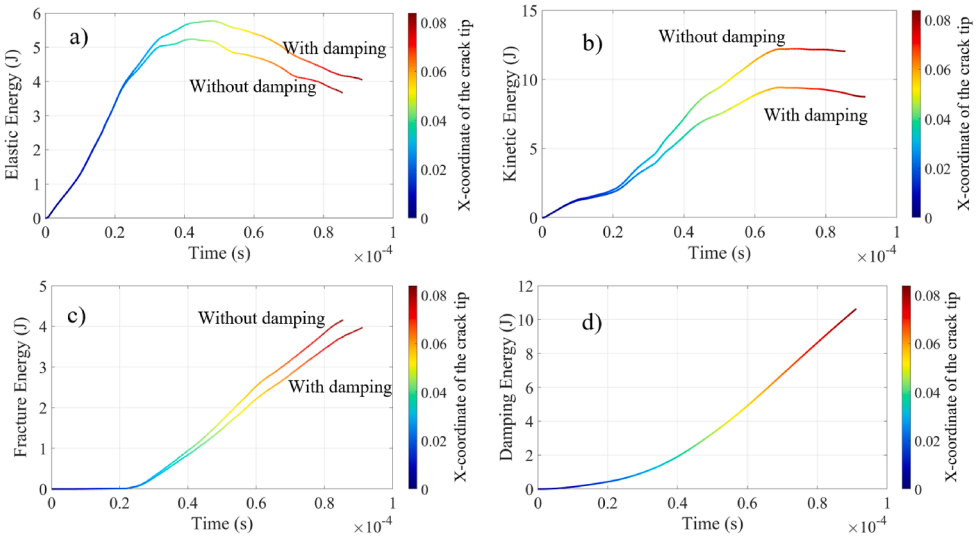

Fig. 29. Energy responses (Kalthoff test).

5. Conclusion

In this paper, we extend our previous work on static crack propagation to the dynamic case, incorporating structural damping effects into the phase-field formulation for brittle fracture. Although phase-field modeling outperforms traditional fracture models in several aspects, it incurs high computational costs due to the required mesh refinement in the damaged zone. A common approach to mitigate this cost is to predefine localized mesh refinement in zones prone to crack propagation. However, even with prior knowledge of the crack path, this method imposes a substantial computational burden before crack initiation. To address this challenge, we applied an automatic adaptive mesh refinement technique for phase-field fracture modeling. The key challenge in adaptive meshing is to determine the optimal location and level of refinement. Phase-field fracture, which evolves naturally within the domain, allows for automatic identification of the refinement zones. A multi-level gradual mesh refinement strategy based on the damage field is applied, where refinement is controlled by evaluating damage values and the field node distances at each step. A center point within an element is classified as a new field node if the node distances in that element exceed the maximum allowable threshold, which is adaptively adjusted based on damage. This method begins with an initial coarse mesh and gradually introduces field nodes as the crack propagates, considerably reducing computational costs. Furthermore, we develop the adaptive phase-field formulation for dynamic crack propagation, explicitly considering damping effects. In this framework, we analyze the energy responses, including external work and other energy components such as kinetic energy, fracture energy, and elastic strain energy. The consistency of the results with experimental observations and the balanced energy responses, confirms the accuracy, stability, and reliability of the proposed approach.

Funding

This research was supported by the Alexander von Humboldt Foundation.

Data availability

Data will be made available on request.

CRediT authorship contribution statement

Hossein Saberi: Writing – original draft, Visualization, Validation, Software, Methodology, Investigation, Formal analysis, Conceptualization; **Alexander Düster:** Writing – review & editing, Validation, Supervision, Methodology, Investigation, Funding acquisition, Formal analysis, Conceptualization.

Declaration of competing interest

The authors declare that they have no known competing financial interests or personal relationships that could have appeared to influence the work reported in this paper.

References

[1] A. Griffith, The phenomena of rupture and flow in solids (1997).
[2] B.N. Cox, H. Gao, D. Gross, D. Rittel, Modern topics and challenges in dynamic fracture, J. Mech. Phys. Solids 53 (3) (2005) 565–596.
[3] T.K. Mandal, V.P. Nguyen, J.Y. Wu, Evaluation of variational phase-field models for dynamic brittle fracture, Eng. Fract. Mech. 235 (2020) 107169.
[4] P. Li, W. Qiu, J. Wu, Y. Wu, K. Hu, L. Zhao, Fourth-order phase field modeling of dynamic fracture in porous brittle materials using an adaptive isogeometric analysis, Eng. Fract. Mech. 315 (2025) 110763.
[5] A.A. Munjiza, The combined finite-discrete element method, John Wiley & Sons, 2004.
[6] D.R. Vyas, J.M. Ottino, R.M. Lueptow, P.B. Umbanhowar, Improved velocity-Verlet algorithm for the discrete element method, Comput. Phys. Commun. (2025) 109524.
[7] A. Antoniou, L. Daudeville, P. Marin, S. Potapov, Extending the discrete element method to account for dynamic confinement and strain-Rate effects for simulating hard impacts on concrete targets, J. Dyn. Behav. Mater. 11 (1) (2025) 119–135.
[8] M. Elices, G. Guinea, J. Gomez, J. Planas, The cohesive zone model: advantages, limitations and challenges, Eng. Fract. Mech. 69 (2) (2002) 137–163.
[9] Z. Shirzadeh, M. Fakoor, Z. Daneshjoo, Simulating delamination in composite laminates with fracture process zone effects: a novel cohesive zone modeling approach, Eng. Fract. Mech. 315 (2025) 110834.
[10] Z.L. Htut, N. Osawa, S. Tanaka, M. Toyosada, Application of equivalent distributed stress concept and modified cohesive zone model in elastic-plastic fracture mechanics analysis of surface cracks, Eng. Fract. Mech. 315 (2025) 110813.
[11] R.W. Macek, S.A. Silling, Peridynamics via finite element analysis, Finite Elem. Anal. Des. 43 (15) (2007) 1169–1178.
[12] D. Abdoh, A new adaptive peridynamic framework for modeling large deformation and fracture behavior of hyperelastic materials, Eng. Fract. Mech. 314 (2025) 110709.
[13] X. Huang, T. Hu, Y. Jin, S. Li, D. Yang, Z. Zheng, The rationality of using dynamic relaxation method for failure simulation in peridynamics, Comput. Methods Appl. Mech. Eng. 438 (2025) 117847.
[14] X. Hu, S. Li, On nonlocal-deformation-field-driven bond-based peridynamics and its inherent nonlocal continuum mechanics, Comput. Methods Appl. Mech. Eng. 435 (2025) 117593.
[15] N. Sukumar, N. Moës, B. Moran, T. Belytschko, Extended finite element method for three-dimensional crack modelling, Int. J. Numer. Methods Eng. 48 (11) (2000) 1549–1570.
[16] V.F. González-Albuixech, E. Giner, A. Gravouil, Analysis of stress intensity factor oscillations in 3D cracks using domain integrals and the extended finite element method, Comput. Methods Appl. Mech. Eng. 436 (2025) 117739.
[17] L. Kachanov, Introduction to continuum damage mechanics, Springer Science & Business Media, 2013.
[18] H. Amor, J.-J. Marigo, C. Maurini, Regularized formulation of the variational brittle fracture with unilateral contact: numerical experiments, J. Mech. Phys. Solids 57 (8) (2009) 1209–1229.
[19] C. Miehe, M. Hofacker, F. Welschinger, A phase field model for rate-independent crack propagation: robust algorithmic implementation based on operator splits, Comput. Methods Appl. Mech. Eng. 199 (45–48) (2010) 2765–2778.
[20] R. de Borst, C.V. Verhoosel, Gradient damage vs phase-field approaches for fracture: similarities and differences, Comput. Methods Appl. Mech. Eng. 312 (2016) 78–94.
[21] D. Dipasquale, G. Sarego, M. Zaccariotto, U. Galvanetto, Dependence of crack paths on the orientation of regular 2D peridynamic grids, Eng. Fract. Mech. 160 (2016) 248–263.
[22] L. Hug, G. Dahan, S. Kollmannsberger, E. Rank, Z. Yosibash, Predicting fracture in the proximal humerus using phase field models, J. Mech. Behav. Biomed. Mater. 134 (2022) 105415.
[23] L. Hug, M. Potten, G. Stockinger, K. Thuro, S. Kollmannsberger, A three-field phase-field model for mixed-mode fracture in rock based on experimental determination of the mode II fracture toughness, Eng. Comput. 38 (6) (2022) 5563–5581.
[24] M.J. Borden, C.V. Verhoosel, M.A. Scott, T.J.R. Hughes, C.M. Landis, A phase-field description of dynamic brittle fracture, Comput. Methods Appl. Mech. Eng. 217 (2012) 77–95.
[25] A. Schlüter, A. Willenbücher, C. Kuhn, R. Müller, Phase field approximation of dynamic brittle fracture, Comput. Mech. 54 (5) (2014) 1141–1161.
[26] V.P. Nguyen, J.-Y. Wu, Modeling dynamic fracture of solids with a phase-field regularized cohesive zone model, Comput. Methods Appl. Mech. Eng. 340 (2018) 1000–1022.
[27] R.J.M. Geelen, Y. Liu, T. Hu, M.R. Tupek, J.E. Dolbow, A phase-field formulation for dynamic cohesive fracture, Comput. Methods Appl. Mech. Eng. 348 (2019) 680–711.
[28] S. Zhou, X. Zhuang, T. Rabczuk, Phase-field modeling of fluid-driven dynamic cracking in porous media, Comput. Methods Appl. Mech. Eng. 350 (2019) 169–198.
[29] H. Ren, X. Zhuang, C. Anitescu, T. Rabczuk, An explicit phase field method for brittle dynamic fracture, Comput. Struct. 217 (2019) 45–56.
[30] L. De Lorenzis, T. Gerasimov, Numerical implementation of phase-field models of brittle fracture, Model. Eng. Using Innovat. Numer. Method. Solid. Fluids (2020) 75–101.
[31] L. Greco, E. Maggiorelli, M. Negri, A. Patton, A. Reali, AT1 fourth-order isogeometric phase-field modeling of brittle fracture, arXiv preprint arXiv:2501.16968 (2025).
[32] R.U. Patil, B.K. Mishra, I. Singh, An adaptive multiscale phase field method for brittle fracture, Comput. Methods Appl. Mech. Eng. 329 (2018) 254–288.
[33] Y. Li, T. Yu, S. Natarajan, T.Q. Bui, A dynamic description of material brittle failure using a hybrid phase-field model enhanced by adaptive isogeometric analysis, Eur. J. Mech.-A/Solids 97 (2023) 104783.
[34] Z. Si, T. Yu, S. Natarajan, An adaptive multi-patch isogeometric phase-field model for dynamic brittle fracture, Comput. Math. Appl. 153 (2024) 1–19.
[35] T. Jin, Z. Li, K. Chen, A novel phase-field monolithic scheme for brittle crack propagation based on the limited-memory BFGS method with adaptive mesh refinement, Int. J. Numer. Methods Eng. 125 (22) (2024) e7572.
[36] A. Pandey, S. Kumar, A multi-level adaptive mesh refinement strategy for unified phase field fracture modeling using unstructured conformal simplices, Comput. Methods Appl. Mech. Eng. 433 (2025) 117514.
[37] L. Greco, J. Kiendl, M. Negri, A. Patton, A. Reali, Fourth-order isogeometric phase-field modeling of dynamic brittle fracture: Numerical study and comparison with second-order models, Comput. Methods Appl. Mech. Eng. 449 (2026) 118513.

[38] H. Saberi, H. Saberi, T.Q. Bui, Y. Heider, M.N. Nguyen, A multi-level adaptive mesh refinement method for phase-field fracture problems, Theor. Appl. Fract. Mech. 125 (2023) 103920.
[39] B. Bourdin, G.A. Francfort, J.-J. Marigo, Numerical experiments in revisited brittle fracture, J. Mech. Phys. Solids 48 (4) (2000) 797–826.
[40] K. Pham, H. Amor, J.-J. Marigo, C. Maurini, Gradient damage models and their use to approximate brittle fracture, Int. J. Damage Mech. 20 (4) (2011) 618–652.
[41] B.E. Rapp, Microfluidics: modeling, mechanics and mathematics, William Andrew, 2016.
[42] R.J. LeVeque, Finite difference methods for ordinary and partial differential equations: steady-state and time-dependent problems, SIAM, 2007.
[43] W. Kim, S.Y. Choi, An improved implicit time integration algorithm: the generalized composite time integration algorithm, Comput. Struct. 196 (2018) 341–354.
[44] S. Erlicher, L. Bonaventura, O.S. Bursi, The analysis of the generalized-α method for non-linear dynamic problems, Comput. Mech. 28 (2) (2002) 83–104.
[45] T. Gerasimov, L. De Lorenzis, A line search assisted monolithic approach for phase-field computing of brittle fracture, Comput. Methods Appl. Mech. Eng. 312 (2016) 276–303.
[46] G. Molnár, A. Gravouil, 2D And 3D abaqus implementation of a robust staggered phase-field solution for modeling brittle fracture, Finite Elem. Anal. Des. 130 (2017) 27–38.
[47] E. Storvik, J.W. Both, J.M. Sargado, J.M. Nordbotten, F.A. Radu, An accelerated staggered scheme for variational phase-field models of brittle fracture, Comput. Methods Appl. Mech. Eng. 381 (2021) 113822.
[48] P. Farrell, C. Maurini, Linear and nonlinear solvers for variational phase-field models of brittle fracture, Int. J. Numer. Methods Eng. 109 (5) (2017) 648–667.
[49] M.J. Borden, T.J. Hughes, C.M. Landis, C.V. Verhoosel, A higher-order phase-field model for brittle fracture: formulation and analysis within the isogeometric analysis framework, Comput. Methods Appl. Mech. Eng. 273 (2014) 100–118.
[50] J.F. Hall, Problems in using the classical rayleigh damping model in nonlinear time-history seismic analyses, Earthquake Eng. Struct. Dyn. 35 (2006) 147–174.
[51] P. Jehel, P. Léger, A. Ibrahimbegovic, Initial versus tangent-stiffness based rayleigh damping in inelastic time history seismic analyses, Comput. Struct. 124 (2013) 1–13.
[52] T. Belytschko, W.K. Liu, B. Moran, K. Elkhodary, Nonlinear finite elements for continua and structures, John wiley & sons, 2014.